Applied Clay Science 143 (2017) 184–191

Contents lists available at ScienceDirect

Applied Clay Science

journal homepage: www.elsevier.com/locate/clay

Research paper

Effects of microstructure of clay minerals, montmorillonite, kaolinite and halloysite, on their benzene adsorption behaviors

Liangliang Deng[a,b], Peng Yuan[a,*], Dong Liu[a], Faïza Annabi-Bergaya[c], Junming Zhou[a,b], Fanrong Chen[a], Zongwen Liu[d]

[a] CAS Key Laboratory of Mineralogy and Metallogeny/Guangdong Provincial Key Laboratory of Mineral Physics and Materials, Guangzhou Institute of Geochemistry, Chinese Academy of Sciences, Guangzhou 510640, China
[b] University of Chinese Academy of Sciences, Beijing 100049, China
[c] CNRS, UMR7374, Interface Confinement Matériaux et Nanostructures, 45071 Orléans, France
[d] School of Chemical and Biomolecular Engineering, University of Sydney, NSW 2006, Australia

ARTICLE INFO

Keywords:
Volatile organic compounds (VOC)
Montmorillonite
Kaolinite
Halloysite
Adsorption

ABSTRACT

Montmorillonite (Mt), kaolinite (Kaol) and halloysite (Hal) are commonly investigated porous clay minerals, but their performance for the adsorption of volatile organic compounds (VOC) was rarely studied. In this work, the dynamic adsorption of benzene, as a model VOC, on Mt, Kaol and Hal was investigated. The effect of the microstructures of the above-mentioned clay minerals on benzene adsorption were explored by comparing the benzene adsorption of the different derivates of these clay minerals, which were obtained by adjusting the interlayer space and the porosity of the clay minerals through heating treatment. Calcium-based montmorillonite (Ca^{2+}-Mt) heated at 120 °C exhibited higher benzene adsorption capacity (141.2 mg/g) than sodium-based montmorillonite (Na^{+}-Mt) heated at 120 °C (87.1 mg/g), because the interlayer distance of Ca^{2+}-Mt was sufficiently large to accommodate the adsorption of benzene. However, for calcined Ca^{2+}-Mt and Na^{+}-Mt, the collapse of their interlayer space resulted in that the interlayer micropores no longer existed and reduced benzene adsorption. Kaol exhibited the lowest benzene adsorption capacity (56.7 mg/g) among the studied clay minerals because its interlayer space was not available for adsorption and because its specific surface area (*SSA*) was relatively small. As a polymorph of Kaol but with a tubular morphology, Hal showed a higher benzene adsorption capacity than Kaol owing to its larger *SSA*. In particular, heating at 120 °C resulted in the increase of the benzene adsorption of Hal, which was ascribed to the exposure of the adsorption sites initially occupied by water molecules. These results demonstrate that the benzene adsorption capacity of the above-mentioned clay minerals was not only highly related to their *SSA* but also strongly affected by their porosity features.

1. Introduction

The emission of volatile organic compounds (VOC), the most common air pollutants from petrochemical, chemical, pharmaceutical and printing industries, has become one of the most serious environmental problems because VOC are toxic, hazardous and even carcinogenic. VOC are the main sources of the photochemical reaction, and they can trigger the formation of secondary organic aerosols that are harmful to human health (Doyle et al., 2004; Ng et al., 2007; Pöschl, 2005). Hence, the treatment of VOC has caused extensive attention. Many technologies, such as adsorption (Dimotakis et al., 1995; Yu et al., 2015a), membrane separation (Belaissaoui et al., 2016), oxidation (Cordi and Falconer, 1997; Kamal et al., 2016) and biological treatments (Doble, 2006) have been proposed for VOC control, among which adsorption is the most applicable technology because of its inexpensive operation cost, low energy and flexibility of adsorption systems (Yu et al., 2015b).

Activated carbon and synthetic zeolites are two types of commonly used adsorbents. Activated carbon is regarded as the most versatile adsorbent owing to its low cost and excellent adsorption capacity. However, its practicability is restricted by drawbacks such as fire risk, pore clogging and difficulties in regeneration (Zhao et al., 1998). Compared to activated carbon, synthetic mesoporous zeolites, such as SBA-15 (Dou et al., 2011) and ZSM-5 (Serrano et al., 2007), have the advantages of controllable pore sizes and good chemical stability in the adsorption of VOC. However, the synthesis process is complex and time-

* Corresponding author at: CAS Key Laboratory of Mineralogy and Metallogeny, Guangzhou Institute of Geochemistry, Chinese Academy of Sciences, Wushan, Guangzhou 510640, China.
E-mail address: yuanpeng@gig.ac.cn (P. Yuan).

http://dx.doi.org/10.1016/j.clay.2017.03.035
Received 15 January 2017; Received in revised form 20 March 2017; Accepted 24 March 2017
Available online 02 April 2017

Table 1
Chemical compositions of Mt, Kaol and Hal.

Sample	Chemical compositions (mass%)										
	SiO_2	Al_2O_3	Fe_2O_3	MgO	CaO	Na_2O	K_2O	MnO	TiO_2	P_2O_5	L.O.I.*
Mt	57.41	15.66	4.93	4.98	2.98	0.11	0.12	0.03	0.31	–	13.33
Kaol	46.66	38.20	0.39	0.10	–	0.04	0.37	–	0.36	0.03	13.60
Hal	41.05	34.97	0.30	0.16	0.23	0.25	0.06	0.03	0.22	–	22.76

L.O.I.* denotes loss on ignition.

consuming (Cundy and Cox, 2003). In addition, the source materials, such as tetraethyl orthosilicate and cetyltrimethyl ammonium bromide are relatively expensive. These shortcomings would be very detrimental for the widespread application of synthetic zeolites. Therefore, many efforts were made to find low cost adsorbents with good adsorption performance and desirable thermal stability. Raw clay minerals have been proposed as alternative adsorbents due to their bidimensional structure and the ample active groups on the surface, such as silanol (Si-OH) and/or aluminol (Al-OH) groups, which were thought as the potential adsorption sites (Hernandez et al., 2004). The feasibility of clay minerals as VOC adsorbents might also be due to their excellent heat resistance and recyclability via thermal desorption. In addition, the wide distribution and abundant reserves of clay minerals make them be the promising environmental adsorbents that can be used in industrial processes.

Montmorillonite, kaolinite and halloysite are three commonly studied clay minerals. Montmorillonite is a 2:1 dioctahedral clay mineral with a layer composed of an alumina octahedral sheet sandwiched between two opposing silica tetrahedral sheets and with more or less hydrated exchangeable cations occurring in the interlayer space. Kaolinite is a 1:1 dioctahedral clay mineral. Each layer contains a silica tetrahedral sheet and an alumina octahedral sheet, which are bound tightly by sharing a common plane of oxygen atoms, and the repeating layers of the mineral along the *c* axis are hydrogen bonded together (Miranda-Trevino and Coles, 2003). Halloysite was first described by Berthier (1826) as a dioctahedral 1:1 clay mineral of the kaolin group. As a hydrated polymorph of kaolinite, halloysite shows some similarities in structure and chemical composition to kaolinite, but the unit layers in halloysite are separated by a monolayer of water molecules (Yuan et al., 2015a). The hydrated form of halloysite is referred to as "halloysite (10 Å)" in which one layer of water molecules is presented in the interlayer space, and where the "10 Å" designation indicates d_{001}-value in the multilayer walls. The dehydrated form of halloysite is referred to as "halloysite (7 Å)", and it may be obtained through the loss of the interlayer water molecules under mild heating and/or in a vacuum environment (Joussein et al., 2005). The dominant morphology of halloysite is tubular, resulting from the wrapping of halloysite layers that is driven by a mismatch between the oxygen-sharing tetrahedral SiO_4 sheet and the adjacent octahedral AlO_6 sheet in the 1:1 layer under favorable crystallization conditions (Singh and Mackinnon, 1996). Generally, the length of the tubular halloysite is 0.02–30 μm, and the external and internal diameters are respectively 30–190 nm and 10–100 nm (Yuan et al., 2008, 2013). These sizes vary in different halloysite deposits (Pasbakhsh et al., 2013). The tubular halloysite has a porous structure, including the cylindrical lumen in the mesopore size range (2–50 nm) and even macropores (> 50 nm) derived from the inner cavity of the tubular halloysite particles (Tan et al., 2013). In spite of the numerous studies on the structure and surface properties of the above-mentioned clay minerals, the mechanism on how the structural characteristics and surface properties of the minerals affect their performance for VOC adsorption has rarely been studied.

In this study, benzene was used as a model organic pollutant to evaluate the VOC dynamic adsorption performance of the above-mentioned clay minerals via the breakthrough curve method. Benzene was selected because it is a commonly used solvent in industrial processes, and it is ranked on top of the list of VOC pollutants. Benzene is toxic and hazardous, and it can enter into the human body through breathing and contacting with the skin, resulting in injury to the nervous system.

The main objectives of this study are to investigate i) the benzene adsorption performance of montmorillonite, kaolinite and halloysite and ii) the relevant adsorption mechanism, such as the effects of the structure and surface properties of these minerals on benzene adsorption. Therefore, different derivates of the above-mentioned minerals were used for benzene adsorption, and they were heated to adjust the hydration state or the interlayer distance of the initial clay minerals. X-ray diffraction (XRD), N_2 adsorption-desorption and diffuse reflectance infrared Fourier transform (DRIFT) spectroscopy methods were adopted to characterize the structural features and surface properties of the clay minerals.

2. Materials and methods

2.1. Materials

Montmorillonite (Mt) was sourced from the Inner Mongolia province of China. Kaolinite (Kaol) was collected from the Guangdong province of China, and halloysite (Hal) from the Shanxi province of China was also used for comparison. A purification method of hand-picking followed by repeated sedimentation was carried out to remove impurities. The chemical compositions of the purified Mt, Kaol and Hal were listed in Table 1.

According to the chemical compositions data (Table 1), the Mt was assigned to calcium-based montmorillonite (denoted as Ca^{2+}-Mt). Sodium-based montmorillonite (denoted as Na^{+}-Mt) was prepared by dispersing Ca^{2+}-Mt in deionized water and by treating it with 0.5 M sodium chloride solution under vigorous stirring at 80 °C for 24 h. The solid phase was then separated from the solution and treated with fresh salt solution, followed by two repetitions of the cation-exchange procedure to enable a complete exchange. The product was repeatedly washed with distilled water and then dried at 60 °C before it was ground to a powder.

Ca^{2+}-Mt and Na^{+}-Mt were heated at 120 °C and 600 °C in a programmed temperature-controlled muffle oven for 3 h and denoted as Ca^{2+}-Mt_x and Na^{+}-Mt_x, where *x* represented the heating temperature in degrees Celsius. Kaol was heated at 120 °C and denoted as $Kaol_{120\ °C}$. The dehydrated Hal was obtained by thermal treatment at 120 °C of the hydrated form of Hal and denoted as $Hal_{120\ °C}$. To prevent the dehydration of the hydrated form of Hal, the hydrated Hal was placed in a water vapor-saturated desiccator at room temperature and denoted as Hal_{RT}. Meanwhile, the heated samples were placed in a desiccator, which was loaded with allochroic silica gel, and vacuumization was performed to maintain a dry environment, thus preventing the re-adsorption of water. All samples were ground by hand for 1 min in an agate mortar.

2.2. Benzene adsorption tests

The benzene adsorption performance of the obtained samples was

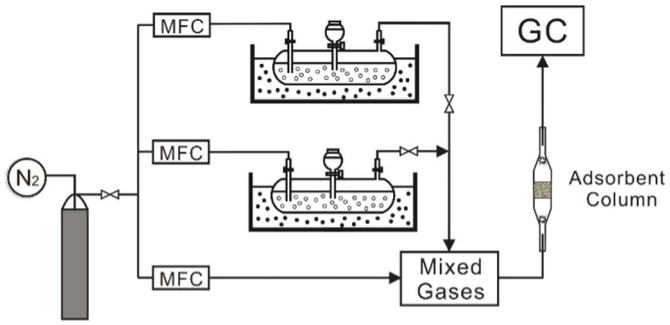

Fig. 1. Schematic diagram of experimental set-up.

evaluated using an in-line gas chromatography apparatus (Fig. 1) (Hu et al., 2009). Before the adsorption process, the samples (except for Hal_{RT}) were heated at 120 °C in a muffle oven for 2 h to remove the water molecules and small organic impurities adsorbed in pores. During the adsorption measurement, the organic saturator with benzene was immersed in a water bath at 30 °C. Each sample weighed approx. 0.5 g and was loaded in a glass column. The column was fed with a dry nitrogen stream containing benzene vapor at 3.00 mL/min. The concentration of benzene in both the column influent and effluent was quantified using a gas chromatograph (Agilent 7820A) with a flame ionisation detector (FID). The experiment was stopped when the adsorption equilibrium reached.

The benzene adsorption capacity (q, mg/g) of the adsorbents was calculated by integrating the area above the acquired breakthrough curve after subtracting the area attributed to the system dead volume, according to the following equation (Eq. (1)):

$$q = \frac{M}{1000m}\int_{t_1}^{t_2} F[C_0 - C_t]dt \quad (1)$$

where M (g/mol) was the molar mass of benzene, m (g) was the initial mass of the adsorbents before the test, t_1 (min) was the breakthrough time without the column, t_2 (min) was the breakthrough time with the packed column, C_0 and C_t (mmol/L) represented the influent and measured effluent benzene concentrations, respectively, and F (mL/min) was the N_2 flow rate. The dead space was obtained by performing blank runs without the column.

The breakthrough curves were fitted using the Yoon and Nelson model (Yoon and Nelson, 1984) (Eq. (2)):

$$t = \tau + \frac{1}{k}\ln\frac{C_t}{C_0 - C_t} \quad (2)$$

where t (min) was the breakthrough time, C_t and C_0 were the outlet and inlet concentrations of the stream through the adsorbent column, τ (min) was the time required for 50% adsorbate breakthrough (time for $0.5C_0$), and k was mass transfer coefficient.

2.3. Characterization methods

The XRD patterns were recorded on a Bruker D8 Advance diffractometer with a Ni filter and Cu-Kα radiation (λ = 0.154 nm) using a generator voltage of 40 kV and a current of 40 mA. The scan rate was 3° (2θ)/min.

N_2 adsorption-desorption isotherms were measured with a Micromeritics ASAP2020 system at liquid-nitrogen temperature. In addition to Hal_{RT}, which was degassed at 30 °C, the other samples were outgassed at 120 °C for 12 h before the measurements. The specific surface areas (*SSA*) of the samples were calculated from the nitrogen adsorption data using the multiple-point Brunauer-Emmett-Teller (BET) method (Brunauer et al., 1938) and the total pore volume (V_{total}) was estimated based on the nitrogen uptake at a relative pressure of approx. 0.99. The Horvath-Kawazoe method (Horvath and Kawazoe, 1983) was adopted to evaluate the micropore size distribution, especially for slit-shaped pores (Ramesh et al., 2016).

The DRIFT characterization was performed on the Praying Mantis™ diffuse reflection accessory (Harrick Scientific Products INC) of a Bruker Vertex-70 Fourier transform infrared spectrometer at room temperature. The DRIFT measurement lasted for 2 min (from the sample loading to the spectrum recording), and the ambient relative humidity was ~30%. The spectra were collected over the range of 600–4000 cm^{-1} with 64 scans and a resolution of 4 cm^{-1} using a KBr background.

3. Results and discussion

3.1. Characterization of the adsorbents

As shown in Fig. 2a, the reflections at approx. 5.8° and 7.0° (*2θ*) are attributed to the (001) characteristic reflections of Ca^{2+}-$Mt_{120\,°C}$ and Na^{+}-$Mt_{120\,°C}$, with d_{001}-values of 1.54 nm and 1.26 nm, respectively. The weak reflection at approx. 27° in all Mt derivates is attributed to quartz impurity (with a content of approx. 3%). The interlayer distances of Ca^{2+}-$Mt_{120\,°C}$ and Na^{+}-$Mt_{120\,°C}$ were obtained by subtracting the thickness of the structural TOT layer unit (approx. 0.96 nm) from d_{001}-value, yielding values of 0.58 nm and 0.30 nm, respectively. The reason of this difference is that the divalent Ca^{2+} has higher hydration power than the monovalent Na^{+}, and Ca^{2+}-Mt has two-layer hydration state in the interlayer space whereas Na^{+}-Mt has one-layer

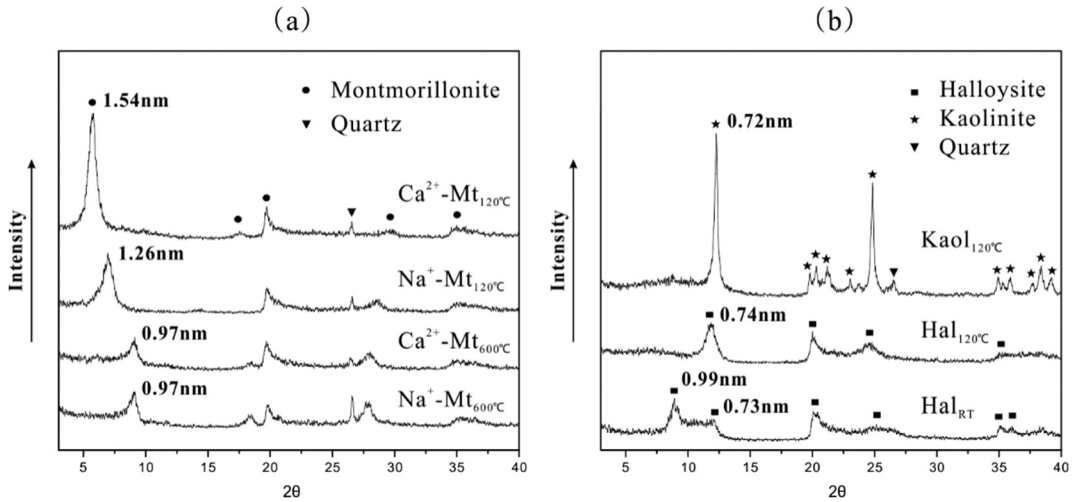

Fig. 2. XRD patterns of (a) Ca^{2+}-$Mt_{120\,°C}$, Ca^{2+}-$Mt_{600\,°C}$, Na^{+}-$Mt_{120\,°C}$ and Na^{+}-$Mt_{600\,°C}$; (b) $Kaol_{120\,°C}$, $Hal_{120\,°C}$ and Hal_{RT}.

hydration state (Morodome and Kawamura, 2009). However, the d_{001}-values of Ca^{2+}-$Mt_{600\,°C}$ and Na^{+}-$Mt_{600\,°C}$ are both 0.97 nm, which indicates that their interlayer distances are negligible. This is due to the collapse of the interlayer space, resulting from the complete dehydration and removal of part of the structural hydroxyl groups after the heat treatment at 600 °C. This result is in agreement with previous studies on calcination of montmorillonite (Wu et al., 2005).

The XRD pattern of $Kaol_{120\,°C}$ shows the main phase of the highly ordered Kaol (Fig. 2b), whose (001) characteristic reflection appears at approx. 12.3° with a d_{001}-value of 0.72 nm. Quartz impurity (with a content of approx. 4%) was found in $Kaol_{120\,°C}$. The thickness of the structural TO layer unit of Kaol was approx. 0.71 nm. Therefore, the interlayer distance of $Kaol_{120\,°C}$, obtained by subtracting the thickness of the structural TO layer unit from the d_{001}-value, was negligible.

Hal occurred mainly in two different polymorphs, the dehydrated and hydrated forms (Guimaraes et al., 2010). Generally, the dehydrated Hal exhibited a very broad and/or weak reflection at ~7.2–7.6 Å owing to the small particle size, tubular morphology and high degree of disorder of layers with various hydration states (Joussein et al., 2005). However, the hydrated Hal exhibited an intense reflection at 10.1 Å, which represented the combined thickness of a monolayer of water molecules (3 Å) and of the structural TO layer unit (7.1 Å). The (001) characteristic reflection of $Hal_{120\,°C}$ (Fig. 2b) appears at approx. 11.7°, and its d_{001}-value is 0.74 nm. These results indicate that $Hal_{120\,°C}$ was completely dehydrated. The XRD pattern of Hal_{RT} (Fig. 2b) presents main d_{001}-values of 0.73 nm and 0.99 nm, reflecting the occurrence of partial dehydration. Previous studies (Kohyama et al., 1978; Yuan, 2016) found that the hydrated Hal could rapidly transform into the dehydrated Hal even under ambient conditions due to its instability.

The nitrogen adsorption-desorption isotherms of all samples are shown in Fig. 3. According to the IUPAC classification refined by Thommes et al. (2015), the isotherms of Mt derivates (Fig. 3a) belong to type II with H3 hysteresis loop, which are characteristic of plate materials with non-rigid slit-like pores (Wang et al., 2015). Furthermore, a slight and steep increase that subsequently lead to a steady adsorption state at a low relative pressure ($P/P_0 < 0.1$) is exhibited on their isotherms (Fig. 3a), indicating the existence of a small amount of micropores. The presence of micropores in the Mt derivates is also verified by their micropore size distributions, which exhibit micropores distribution at the range of approx. 0.3–0.8 nm (Fig. 4a). The micropores of Ca^{2+}-$Mt_{600\,°C}$ and Na^{+}-$Mt_{600\,°C}$ are attributed to the interparticle micropores, of which the micropores distributions were centered at 0.57 nm and 0.58 nm, respectively (Fig. 4a), because the interlayer space of Ca^{2+}-$Mt_{600\,°C}$ and Na^{+}-$Mt_{600\,°C}$ collapsed, which led to the disappearance of the interlayer micropores. In contrast, the micropores of Ca^{2+}-$Mt_{120\,°C}$ and Na^{+}-$Mt_{120\,°C}$ were derived from both interparticle micropores and interlayer micropores. Additionally, the micropores distribution of Ca^{2+}-$Mt_{120\,°C}$ is centered at approx. 0.60 nm, which matches well with its interlayer distance (0.58 nm). This size is similar to the primary micropores distribution of Ca^{2+}-$Mt_{600\,°C}$ (0.57 nm) and Na^{+}-$Mt_{600\,°C}$ (0.58 nm), indicating that the pore size of interlayer micropores of Ca^{2+}-$Mt_{120\,°C}$ was close to that of its interparticle micropores. Unlike Ca^{2+}-$Mt_{120\,°C}$, the main micropores distribution of Na^{+}-$Mt_{120\,°C}$ is at 0.49 nm, which is due to the relatively small interlayer distance (0.30 nm) of Na^{+}-$Mt_{120\,°C}$.

The specific surface area (*SSA*) of Na^{+}-$Mt_{120\,°C}$ (107.7 m^2/g) is larger than that of Ca^{2+}-$Mt_{120\,°C}$ (69.5 m^2/g) (Table 2). This result is due to that the interparticle microporosity of Na^{+}-$Mt_{120\,°C}$ was more developed than that of Ca^{2+}-$Mt_{120\,°C}$, although the interlayer microporosity of Na^{+}-$Mt_{120\,°C}$ was less developed than Ca^{2+}-$Mt_{120\,°C}$. A similar result was obtained in a previous study (Neaman et al., 2003), which investigated the effect of interlayer exchangeable cations on the *SSA* of Mt and found that the *SSA* of Na^{+}-Mt was higher than that of Ca^{2+}-Mt. However, the *SSA* of Ca^{2+}-$Mt_{600\,°C}$ and Na^{+}-$Mt_{600\,°C}$ is decreased and are nearly equivalent (Table 2). The reason is that their interlayer space collapsed and the interlayer micropores disappeared.

Fig. 3b displays the nitrogen adsorption-desorption isotherms of $Kaol_{120\,°C}$, Hal_{RT} and $Hal_{120\,°C}$. The isotherm of $Kaol_{120\,°C}$ exhibits a similar shape to those of Mt derivates but with a much minor hysteresis loop. The isotherms of Hal_{RT} and $Hal_{120\,°C}$ were classified as type IV isotherms with H3 hysteresis loop (Zhang et al., 2012a). The hysteresis in the isotherms is associated with the filling through capillary condensation and emptying of mesopores, which primarily originated from the mesoscopic lumen.

$Kaol_{120\,°C}$ shows the smallest *SSA* (17.9 m^2/g) among all samples (Table 2). In addition, its microporosity is too minor to be detected, so that the micropore size distribution curve of $Kaol_{120\,°C}$ is not presented. The *SSA* of $Hal_{120\,°C}$ is 58.4 m^2/g, obviously larger than that of Hal_{RT} (27.8 m^2/g). This result is due to the exposure of adsorption sites that were initially occupied by water. Another possible reason for that is the formation of slit-shaped pores after the dehydration of Hal, which is due to the separation of the rolled layers that were originally connected tightly to each other (Yuan, 2016). The micropores distributions of Hal_{RT} and $Hal_{120\,°C}$ confirm the existence of slit-shaped pores (Fig. 4b). And the micropores distribution of Hal_{RT} centered at 0.55 nm is attributed to slit-shaped pores due to partial dehydration. Meanwhile,

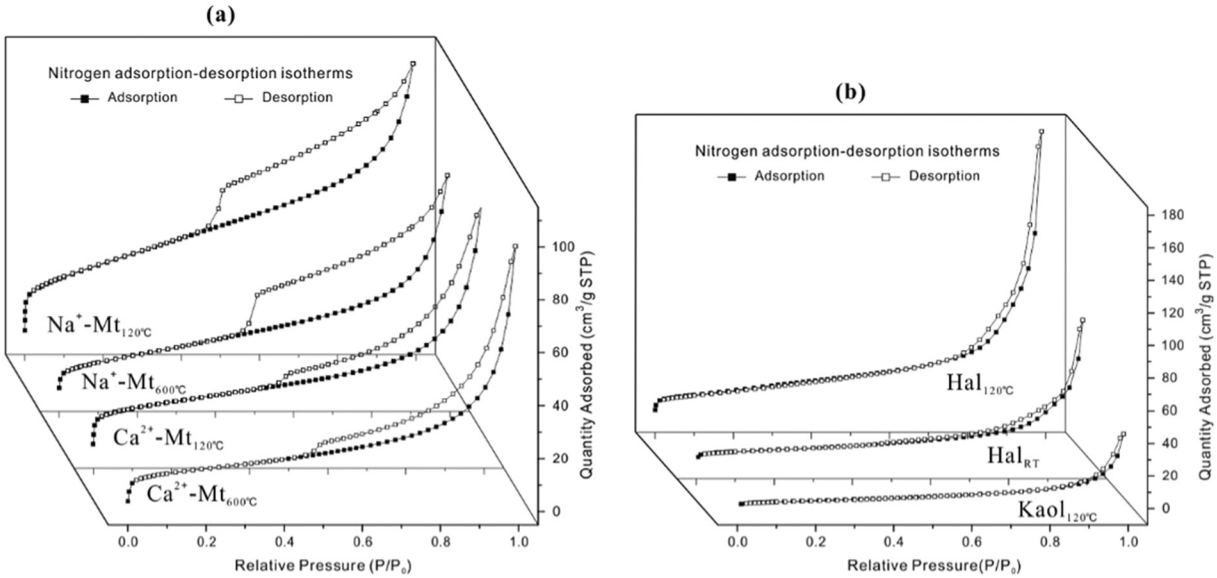

Fig. 3. N_2 adsorption-desorption isotherms of (a) Ca^{2+}-$Mt_{120\,°C}$, Ca^{2+}-$Mt_{600\,°C}$, Na^{+}-$Mt_{120\,°C}$ and Na^{+}-$Mt_{600\,°C}$; (b) $Kaol_{120\,°C}$, Hal_{RT} and $Hal_{120\,°C}$.

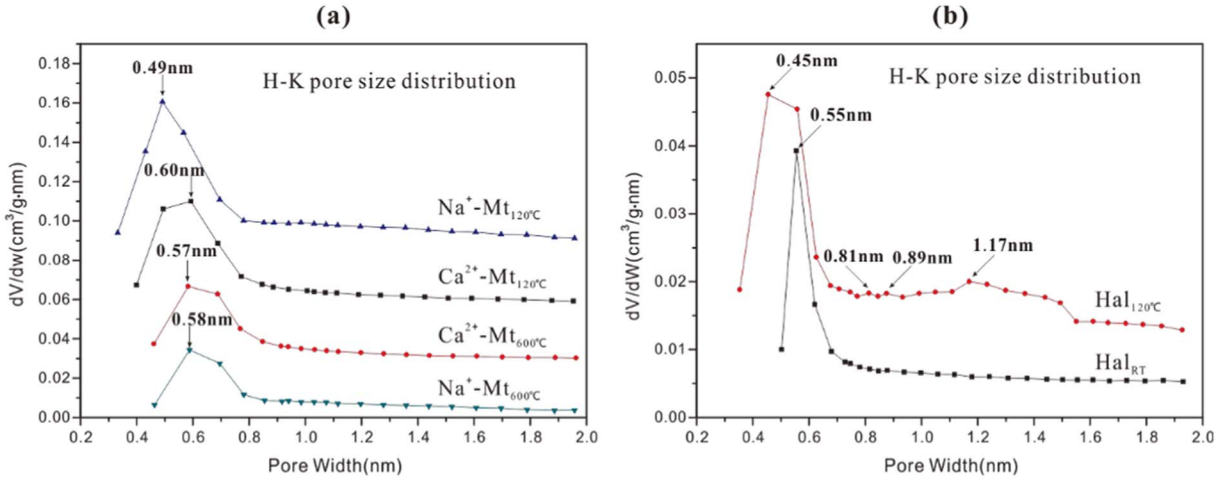

Fig. 4. Horvath-Kawazoe (H-K) pore size distribution (PSD) curves of (a) Ca^{2+}-$Mt_{120\ ^\circ C}$, Ca^{2+}-$Mt_{600\ ^\circ C}$, Na^{+}-$Mt_{120\ ^\circ C}$ and Na^{+}-$Mt_{600\ ^\circ C}$; (b) Hal_{RT} and $Hal_{120\ ^\circ C}$.

Table 2
Porosity parameters, dynamic adsorption capacity (q) and Yoon and Nelson equation parameters for benzene adsorption on various adsorbents.

Sample	*SSA* (m^2/g)	V_{total} (cm^3/g)	q (mg/g)	Yoon and Nelson parameters		
				τ(min)	k	R^2
Ca^{2+}-$Mt_{120\ ^\circ C}$	69.5	0.119	141.2	46.8	0.201	0.987
Na^{+}-$Mt_{120\ ^\circ C}$	107.7	0.143	87.1	30.0	0.210	0.990
Ca^{2+}-$Mt_{600\ ^\circ C}$	57.1	0.115	77.5	25.8	0.212	0.974
Na^{+}-$Mt_{600\ ^\circ C}$	60.4	0.109	67.9	24.1	0.240	0.991
$Kaol_{120\ ^\circ C}$	17.9	0.050	56.7	17.7	0.640	0.972
$Hal_{120\ ^\circ C}$	58.4	0.270	68.1	21.2	0.241	0.964
Hal_{RT}	27.8	0.098	62.7	19.5	0.313	0.960

due to completely dehydration, the main micropores distribution center of $Hal_{120\ ^\circ C}$ shifted to 0.45 nm, and some minor micropores distributions centered at 0.81, 0.89 and 1.17 nm appear. This result indicated that much more micropores were emerged and the sizes of the micropores were non-uniform.

3.2. Benzene adsorption

3.2.1. Benzene adsorption on montmorillonite

The breakthrough curves of all samples (Fig. 5) were used to evaluate their dynamic benzene adsorption capacity (q value, Table 2). Ca^{2+}-$Mt_{120\ ^\circ C}$ exhibits the best benzene adsorption performance (Fig. 5a), and its adsorption capacity (q value) reaches 141.2 mg/g (Table 2). However, the q value of Na^{+}-$Mt_{120\ ^\circ C}$ is only 87.1 mg/g even though it has a larger *SSA* (107.7 mg/g) than Ca^{2+}-$Mt_{120\ ^\circ C}$. This result suggests that the benzene adsorption capacity of Mt is not directly correlated with the *SSA*. Instead, the benzene adsorption of Mt was highly related to its interlayer microporosity. As aforementioned, the interlayer distance of Ca^{2+}-$Mt_{120\ ^\circ C}$ is 0.58 nm, which is close to the kinetic diameter of the benzene molecule (0.59 nm) and obviously larger than the van der Waals diameter of carbon atom (0.34 nm), representing the smallest one-dimensional size that a benzene molecule could adopt. As a result, considerable amounts of benzene molecules could be adsorbed into the interlayer micropores of Ca^{2+}-$Mt_{120\ ^\circ C}$. However, the interlayer distance of Na^{+}-$Mt_{120\ ^\circ C}$ is only approx. 0.30 nm, even smaller than the van der Waals diameter of the carbon atom. Therefore, only a small amount of the interlayer micropores of Na^{+}-$Mt_{120\ ^\circ C}$ is available for benzene adsorption, resulting in the relatively lower benzene adsorption capacity. In this case, micropores exhibited a sieving effect (Luebbers et al., 2010) for benzene adsorption, i.e., benzene adsorption in micropores occurred only when the size of micropores was larger than the diameter of benzene molecule. Similarly, Zhang et al., (2012b) compared the dynamic adsorption characteristics of toluene on different porous materials and found that the presence of the micropores directly led to an increase in the toluene adsorption capacity. Liu et al. (2013) investigated the methane (CH_4) adsorption on Mt, and they also found that the

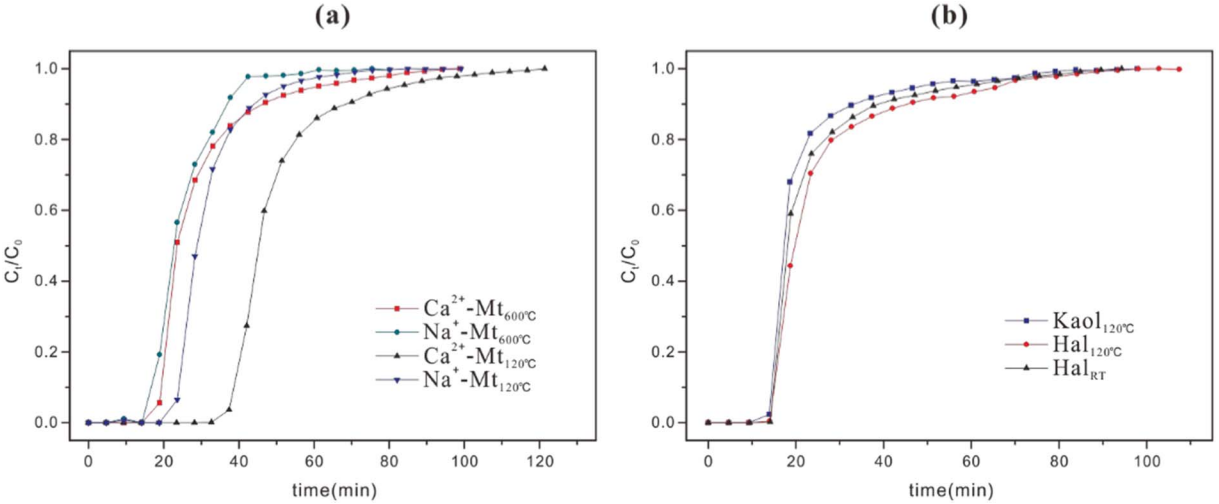

Fig. 5. Breakthrough curves of (a) Ca^{2+}-$Mt_{120\ ^\circ C}$, Ca^{2+}-$Mt_{600\ ^\circ C}$, Na^{+}-$Mt_{120\ ^\circ C}$ and Na^{+}-$Mt_{600\ ^\circ C}$; (b) $Kaol_{120\ ^\circ C}$, Hal_{RT} and $Hal_{120\ ^\circ C}$.

CH_4 adsorption in the interlayer space of Mt. However, the CH_4 adsorption was performed at high pressure (up to 18.0 MPa), because the CH_4 adsorption on clay minerals could not reach saturation at low pressure. Unlike that case, the benzene adsorption in the interlayer space of Mt occurred at atmospheric pressure in this work, which indicates the relatively mild condition of benzene adsorption in Ca^{2+}-$Mt_{120\ °C}$.

For Ca^{2+}-$Mt_{600\ °C}$ and Na^{+}-$Mt_{600\ °C}$, their *q* values are decreased to 77.5 mg/g and 67.9 mg/g (Table 2), respectively. This result is due to that the interlayer space of Ca^{2+}-$Mt_{600\ °C}$ and Na^{+}-$Mt_{600\ °C}$ collapsed and their interlayer micropores disappeared; therefore, they no longer provided interlayer space for benzene adsorption. Owing to the vanishing of the interlayer micropores, the benzene adsorption reaction of Ca^{2+}-$Mt_{600\ °C}$ and Na^{+}-$Mt_{600\ °C}$ was mainly caused by micropore filling in the interparticle space and by external surface adsorption.

Ca^{2+}-$Mt_{120\ °C}$ shows the highest benzene adsorption capacity, but its mass transfer coefficient *k* (0.201, Table 2) is the smallest among those of the Mt derivates. This result indicates that Ca^{2+}-$Mt_{120\ °C}$ has the greatest diffusion and mass transfer resistance in the benzene adsorption process, because *k* value is positively related to the diffusion and mass transfer resistance of the absorbent (Hu et al., 2009). This strong diffusion and mass transfer resistance is attributed to the presence of interlayer micropores in Ca^{2+}-$Mt_{120\ °C}$, which made the penetration of benzene through the sample be much more difficult, because of the benzene adsorption in interlayer micropores.

To detect the interactions between benzene and the clay minerals, DRIFT characterization was performed. The obtained sample after Ca^{2+}-$Mt_{120\ °C}$ had adsorbed benzene was named as Ca^{2+}-$Mt_{120\ °C}$-Ben. As shown in Fig. 6b, some new vibrational bands, including the C—H stretching vibrational bands (~3093, ~3070 and ~3039 cm^{-1}) and the C=C stretching vibrational band (~1479 cm^{-1}) of the aromatic rings (Abdou et al., 2004; Boujday et al., 2010; Du et al., 2002; Ghorab et al., 2004; Todorova and Su, 2003), appear in the DRIFT spectrum of Ca^{2+}-$Mt_{120\ °C}$-Ben compared with that of Ca^{2+}-$Mt_{120\ °C}$ (Fig. 6a). This result indicates the adsorption of benzene on Ca^{2+}-$Mt_{120\ °C}$. Furthermore, compared with the DRIFT spectrum of Ca^{2+}-$Mt_{120\ °C}$, the structural OH vibrational band (~3625 cm^{-1}), the OH stretching (~3412 cm^{-1}) and bending (~1640 cm^{-1}) vibrations of the adsorbed water and the bending vibration of Al-OH (~917 cm^{-1}) in the DRIFT spectrum of Ca^{2+}-$Mt_{120\ °C}$-Ben (Liu et al., 2011) remained entirely unchanged. This result indicates that chemical bonds were not formed between benzene and the hydroxyl groups of Ca^{2+}-$Mt_{120\ °C}$, which implies that the type of benzene adsorption on Mt is physical adsorption.

3.2.2. Benzene adsorption on kaolinite and halloysite

Fig. 4b exhibits the benzene breakthrough curves of $Kaol_{120\ °C}$, Hal_{RT} and $Hal_{120\ °C}$. $Kaol_{120\ °C}$ shows the poorest benzene adsorption performance. The primary reason for this is that the benzene adsorption on $Kaol_{120\ °C}$ only occurred at the external surface, since the microporosity of $Kaol_{120\ °C}$ is small as described earlier. Furthermore, the *SSA* of $Kaol_{120\ °C}$ (17.9 m^2/g) is the smallest among all samples, corresponding to the least amount of surface sites for adsorption. As a result, $Kaol_{120\ °C}$ shows the lowest *q* value (56.7 mg/g) and the largest mass transfer coefficient *k* (0.640).

The benzene adsorption performance of Hal is quite different from that of Kaol, although it is a polymorph of Kaol. The benzene adsorption capacity of Hal_{RT} (62.7 mg/g) is higher than that of $Kaol_{120\ °C}$ (56.7 mg/g), which is due to that Hal_{RT} has a larger *SSA* (27.8 m^2/g) than $Kaol_{120\ °C}$ (17.9 m^2/g). Note that, the slit-shaped micropores in Hal_{RT}, generated by partial dehydration, might not contribute to the benzene adsorption, because the size (0.55 nm) of such micropores is smaller than the kinetic diameter of the benzene molecule (0.59 nm) so that they could not be available for benzene adsorption. Similar to Kaol, the benzene adsorption of Hal_{RT} is mainly caused by external surface adsorption.

The benzene adsorption capacity of $Hal_{120\ °C}$ is 68.1 mg/g, slightly higher than that of Hal_{RT}. This result is due to that the removal of water molecules for $Hal_{120\ °C}$ allowed adsorption of more benzene molecules. Furthermore, the *SSA* of $Hal_{120\ °C}$ (58.4 m^2/g) is distinctly larger than that of Hal_{RT} (27.8 m^2/g), which means that the increase of benzene adsorption capacity of $Hal_{120\ °C}$ relative to that of Hal_{RT} was not as large as the increase of the *SSA* of $Hal_{120\ °C}$ relative to that of Hal_{RT}. This result is due to that, the pore size of the non-uniform slit-shaped micropores resulting from dehydration is large enough to host nitrogen adsorption but not sufficiently large to accommodate benzene adsorption because of the size difference of nitrogen and benzene. Therefore, it is very likely that the improvement in the benzene adsorption performance of $Hal_{120\ °C}$ compared with Hal_{RT} is primarily due to the exposure of adsorption sites in the mesoscopic lumen that were originally occupied by water molecules.

In the DRIFT spectra of Kaol samples (Fig. 6e and f), no difference is shown between the DRIFT spectrum of $Kaol_{120\ °C}$ and that of $Kaol_{120\ °C}$-Ben, the benzene-adsorbed $Kaol_{120\ °C}$, indicating that the amount of benzene molecules on the surface of $Kaol_{120\ °C}$-Ben was too small to be detected. This is due to the lowest benzene adsorption capacity of $Kaol_{120\ °C}$ and/or the rapid desorption process indicated by its largest mass transfer coefficient *k* (0.640, Table 2), which was nearly 2.5 and 3.2 times as large as those of $Hal_{120\ °C}$ (0.241) and Ca^{2+}-$Mt_{120\ °C}$

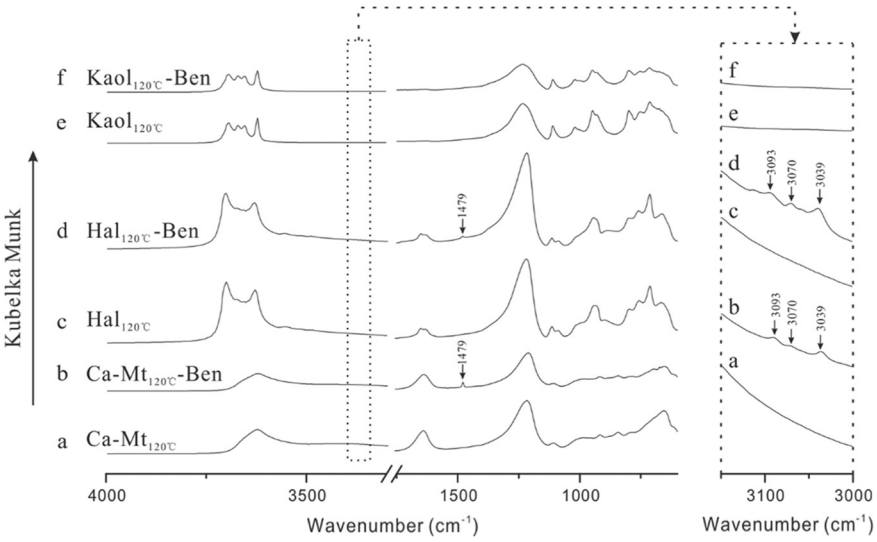

Fig. 6. DRIFT spectra of Ca^{2+}-$Mt_{120\ °C}$, $Kaol_{120\ °C}$ and $Hal_{120\ °C}$ (before and after benzene adsorption).

(0.201), respectively. Unlike Kaol, the characteristic vibrational bands of benzene, including the C—H stretching (~3093, ~3070 and ~3039 cm^{-1}) and the C=C stretching (~1479 cm^{-1}) of the aromatic rings appear on the DRIFT spectrum of $Hal_{120\ °C}$-Ben. This result confirms the benzene adsorption. However, the vibrational bands of hydroxyl groups of halloysite (Kloprogge, 2016; Theng et al., 1982), including the stretching of inner-surface hydroxyl groups (~3701 cm^{-1}), the stretching of inner hydroxyl groups (~3629 cm^{-1}), the O—H deformation of absorbed water (~1651 cm^{-1}) and the O—H deformation of inner-surface hydroxyl groups (~944 cm^{-1}), remains unchanged as compared with $Hal_{120\ °C}$. Accordingly, the type of benzene adsorption on Kaol and Hal also belongs to physical adsorption.

3.2.3. Main factors that affect the benzene adsorption capacity on layered clay minerals

According to the above results, benzene adsorption behaviors of Mt, Kaol and Hal are different. Benzene adsorption is not only affected by their *SSA* values but also by the porosity characteristics. For Mt, the representative swelling clay mineral, its adsorption performance is strongly affected by the amount of the available interlayer micropores, and more available interlayer micropores result in better benzene adsorption performance. Moreover, the interlayer microporosity is affected by the interlayer exchangeable cations and heating temperature. The interlayer distance of Mt with monovalent cations (such as sodium) in the interlayer space is small, leading to minor interlayer microporosity. In contrast, the Mt with divalent cations (such as calcium) in the interlayer space has considerable interlayer micropores that are available for benzene adsorption.

For Kaol and Hal, the benzene adsorption in the interlayer space is not applicable to these clay minerals because they have non-expandable interlayer space. Instead, the benzene adsorption of Kaol and Hal mainly occur at external surface, and their benzene adsorption performance is determined by the *SSA* values of them. In addition, heating treatment could affect the benzene adsorption by removing the amount of adsorbed water on the surface of Kaol and Hal. For Hal, the slit-shaped micropores resulted from dehydration also influences the benzene adsorption. All these factors should be taken into account for the actual applications of these minerals as VOC adsorbents.

The benzene adsorptions on the studied clay minerals in the present work are all attributed to physical adsorption. This is an advantageous feature that would be useful for the regeneration of these clay minerals as adsorbents of VOC, since they could be readily regenerated through thermal desorption. In particular, compared with activated carbon that is combustible and would be with fire risk in the thermal desorption process, these studied clay minerals have excellent heat resistance so that their combustion risk is low. However, more in-depth investigations on the thermal regeneration of the studied clay minerals, beyond the scope of this study, needs to be conducted in future.

Studies on the dynamic VOC adsorption by clay minerals in literature are rare. A comparison of the results in these studies and those obtained in this work in somewhat difficult. For example, Cheng and Reinhard (2006) investigated the performance of Kaol for the dynamic adsorption of trichloroethylene, and found the adsorption was mainly occurred on the external surface of Kaol. However, the trichloroethylene adsorption capacity is only 0.08 mg/g, much lower than the benzene adsorption capacity in this work. This result might be due to the size difference of trichloroethylene and benzene. In addition, dynamic adsorption of benzene on some other minerals were also reported. For example, Yuan et al. (2015b) investigated the dynamic adsorption of benzene by diatomite (Dt), and found that the benzene adsorption capacity of Dt reached 73.7 mg/g, which is higher than that of $Kaol_{120\ °C}$ or $Hal_{120\ °C}$ in this work. This might be attributed to the existence of some micropores in Dt (Wang et al., 2009).

Other studies dealt with synthesized porous materials such as activated carbon and porous silica. Some of them presented very high benzene adsorption capacity (e.g., 173.9 mg/g for ZSM-5 with a *SSA* of 330.7 m^2/g, 98.4 mg/g for KIT-6 with a *SSA* of 912 m^2/g, and 120 mg/g for activated carbon with a *SSA* of 883 m^2/g,) (Dou et al., 2011; Lillo-Ródenas et al., 2005; Yuan et al., 2015b); and others reported relatively low benzene adsorption capacity for some other synthetic silica materials (e.g., 71.1 mg/g for SBA-15 with a *SSA* of 698 m^2/g, 79.7 mg/g for MCM-41 with a *SSA* of 1088 m^2/g, and 76.5 mg/g for MCM-48 with a *SSA* of 1210 m^2/g) (Dou et al., 2011). This difference implies that the applied methods and instruments might substantially affect the assessment of the benzene adsorption of materials so that much care should be taken during a comparison between different materials. Despite that, benzene adsorption of the above-mentioned clay minerals seems sometimes lower than the synthetic porous materials with high *SSA*, the potential of clay minerals for VOC adsorption, which are much more readily obtainable than the synthetic materials, merits further investigations in future.

4. Conclusions

In this study, the benzene dynamic adsorption performance of montmorillonite, kaolinite and halloysite and the relevant adsorption mechanism were investigated. Mt showed the best benzene adsorption performance, while the benzene adsorption of Kaol was the poorest. The microporosity characteristics significantly affected the benzene adsorption of these clay minerals. For Mt, the benzene adsorption was determined not only the *SSA* of Mt but also the development of interlayer micropores, which is highly sensitive to the types of interlayer cations and the heating conditions. Unlike Mt, for Kaol and Hal, the interlayer micropores were unavailable for the benzene molecules, and the benzene adsorption was mainly influenced by external surface adsorption that was determined by the *SSA* values of clay minerals.

In summary, the research results of this work demonstrate that these clay minerals have good benzene adsorption capacity and have potential for being used as effective VOC adsorbents. Adjusting the amount of micropores and adsorption sites of clay minerals might be an effective way to improve the VOC adsorption performance of clay minerals.

Acknowledgements

Financial support from the National Natural Science Foundation of China (Grant Nos. 41472045, 41672042 and 41472044), the Team Project of the Natural Science Foundation of Guangdong Province, China (Grant No. S2013030014241), Youth Innovation Promotion Association CAS and the CAS-SAFEA International Partnership Program for Creative Research Teams (Grant No. 20140491534) are gratefully acknowledged. This is a contribution No. IS-2369 from GIGCAS.

References

Abdou, I.M., Saleh, A.M., Zohdi, H.F., 2004. Synthesis and antitumor activity of 5-trifluoromethyl-2, 4-dihydropyrazol-3-one nucleosides. Molecules 9, 109–116.
Belaissaoui, B., Le Moullec, Y., Favre, E., 2016. Energy efficiency of a hybrid membrane/condensation process for VOC (volatile organic compounds) recovery from air: a generic approach. Energy 95, 291–302.
Berthier, P., 1826. Analyse de l'halloysite. Ann. Chim. Phys. 32, 332–335.
Boujday, S., Nasri, S., Salmain, M., Pradier, C.M., 2010. Surface IR immunosensors for label-free detection of benzo[a]pyrene. Biosens. Bioelectron. 26, 1750–1754.
Brunauer, S., Emmett, P.H., Teller, E., 1938. Adsorption of gases in multimolecular layers. J. Am. Chem. Soc. 60, 309–319.
Cheng, H., Reinhard, M., 2006. Sorption of trichloroethylene in hydrophobic micropores of dealuminated Y zeolites and natural minerals. Environ. Sci. Technol. 40, 7694–7701.
Cordi, E.M., Falconer, J.L., 1997. Oxidation of volatile organic compounds on a Ag/Al_2O_3 catalyst. Appl. Catal. A Gen. 151, 179–191.
Cundy, C.S., Cox, P.A., 2003. The hydrothermal synthesis of zeolites: history and development from the earliest days to the present time. Chem. Rev. 103, 663–702.
Dimotakis, E., Cal, M., Economy, J., Rood, M., Larson, S., 1995. Chemically treated

activated carbon cloths for removal of volatile organic carbons from gas streams: evidence for enhanced physical adsorption. Environ. Sci. Technol. 29, 1876–1880.
Doble, M., 2006. Biological treatment of VOCs. Chem. Eng. (N. Y.) 113, 35–41.
Dou, B., Hu, Q., Li, J., Qiao, S., Hao, Z., 2011. Adsorption performance of VOCs in ordered mesoporous silicas with different pore structures and surface chemistry. J. Hazard. Mater. 186, 1615–1624.
Doyle, M., Sexton, K.G., Jeffries, H., Bridge, K., Jaspers, I., 2004. Effects of 1, 3-butadiene, isoprene, and their photochemical degradation products on human lung cells. Environ. Health Perspect. 1488–1495.
Du, Y., Wang, H., Chen, S., 2002. Study on alkylation of benzene with ethylene over β-zeolite catalyst to ethylbenzene by in situ IR. J. Mol. Catal. A Chem. 179, 253–261.
Ghorab, M., Ismail, Z.H., Abdel-Gawad, S.M., Aziem, A.A., 2004. Antimicrobial activity of amino acid, imidazole, and sulfonamide derivatives of pyrazolo [3, 4-d] pyrimidine. Heteroat. Chem. 15, 57–62.
Guimaraes, L., Enyashin, A.N., Seifert, G., Duarte, H.A., 2010. Structural, electronic, and mechanical properties of single-walled halloysite nanotube models. J. Phys. Chem. C 114, 11358–11363.
Hernandez, M., Velasco, J., Asomoza, M., Solís, S., Rojas, F., Lara, V., 2004. Adsorption of benzene, toluene, and p-xylene on microporous SiO_2. Ind. Eng. Chem. Res. 43, 1779–1787.
Horvath, G., Kawazoe, K., 1983. Method for the calculation of effective pore size distribution in molecular sieve carbon. J. Chem. Eng. Jpn. 16, 470–475.
Hu, Q., Li, J.J., Hao, Z.P., Li, L.D., Qiao, S.Z., 2009. Dynamic adsorption of volatile organic compounds on organofunctionalized SBA-15 materials. Chem. Eng. J. 149, 281–288.
Joussein, E., Petit, S., Churchman, J., Theng, B., Righi, D., Delvaux, B., 2005. Halloysite clay minerals-a review. Clay Miner. 40, 383–426.
Kamal, M.S., Razzak, S.A., Hossain, M.M., 2016. Catalytic oxidation of volatile organic compounds (VOCs)-a review. Atmos. Environ. 140, 117–134.
Kloprogge, J.T., 2016. Characterisation of halloysite by spectroscopy. In: Yuan, P., Thill, A., Bergaya, F. (Eds.), Nanosized Tubular Clay Minerals. Elsevier, Amsterdam, pp. 116–136 (Chapter 6).
Kohyama, N., Fukushima, K., Fukami, A., 1978. Observation of the hydrated form of tubular halloysite by an electron microscope equipped with an environmental cell. Clay Clay Miner. 26, 25–40.
Lillo-Ródenas, M.A., Cazorla-Amorós, D., Linares-Solano, A., 2005. Behaviour of activated carbons with different pore size distributions and surface oxygen groups for benzene and toluene adsorption at low concentrations. Carbon 43, 1758–1767.
Liu, D., Yuan, P., Liu, H., Cai, J., Qin, Z., Tan, D., Zhou, Q., He, H., Zhu, J., 2011. Influence of heating on the solid acidity of montmorillonite: a combined study by DRIFT and Hammett indicators. Appl. Clay Sci. 52, 358–363.
Liu, D., Yuan, P., Liu, H., Li, T., Tan, D., Yuan, W., He, H., 2013. High-pressure adsorption of methane on montmorillonite, kaolinite and illite. Appl. Clay Sci. 85, 25–30.
Luebbers, M.T., Wu, T., Shen, L., Masel, R.I., 2010. Effects of molecular sieving and electrostatic enhancement in the adsorption of organic compounds on the zeolitic imidazolate framework ZIF-8. Langmuir 26, 15625–15633.
Miranda-Trevino, J.C., Coles, C.A., 2003. Kaolinite properties, structure and influence of metal retention on pH. Appl. Clay Sci. 23, 133–139.
Morodome, S., Kawamura, K., 2009. Swelling behavior of Na-and Ca-montmorillonite up to 150 °C by in situ X-ray diffraction experiments. Clay Clay Miner. 57, 150–160.
Neaman, A., Pelletier, M., Villieras, F., 2003. The effects of exchanged cation, compression, heating and hydration on textural properties of bulk bentonite and its corresponding purified montmorillonite. Appl. Clay Sci. 22, 153–168.
Ng, N., Kroll, J., Chan, A., Chhabra, P., Flagan, R., Seinfeld, J., 2007. Secondary organic aerosol formation from m-xylene, toluene, and benzene. Atmos. Chem. Phys. 7, 3909–3922.
Pasbakhsh, P., Churchman, G.J., Keeling, J.L., 2013. Characterisation of properties of various halloysites relevant to their use as nanotubes and microfibre fillers. Appl. Clay Sci. 74, 47–57.
Pöschl, U., 2005. Atmospheric aerosols: composition, transformation, climate and health effects. Angew. Chem. Int. Ed. 44, 7520–7540.
Ramesh, K., Reddy, K.S., Rashmi, I., Biswas, A., Islam, K., 2016. Horvath-Kawazoe model based evaluation of pore volume of nanoporous clinoptilolite. Commun. Soil Sci. Plant Anal. 47, 1622–1629.
Serrano, D.P., Calleja, G., Botas, J.A., Gutierrez, F.J., 2007. Characterization of adsorptive and hydrophobic properties of silicalite-1, ZSM-5, TS-1 and Beta zeolites by TPD techniques. Sep. Purif. Technol. 54, 1–9.
Singh, B., Mackinnon, I.D., 1996. Experimental transformation of kaolinite to halloysite. Clay Clay Miner. 44, 825–834.
Tan, D., Yuan, P., Annabi-Bergaya, F., Yu, H., Liu, D., Liu, H., He, H., 2013. Natural halloysite nanotubes as mesoporous carriers for the loading of ibuprofen. Microporous Mesoporous Mater. 179, 89–98.
Theng, B., Russell, M., Churchman, G., Parfitt, R., 1982. Surface properties of allophane, halloysite, and imogolite. Clay Clay Miner. 30, 143–149.
Thommes, M., Kaneko, K., Neimark, A.V., Olivier, J.P., Rodriguez-Reinoso, F., Rouquerol, J., Sing, K.S., 2015. Physisorption of gases, with special reference to the evaluation of surface area and pore size distribution (IUPAC Technical Report). Pure Appl. Chem. 87, 1051–1069.
Todorova, S., Su, B.-L., 2003. Propane as alkylating agent for benzene alkylation on bimetal Ga and Pt modified H-ZSM-5 catalysts: FTIR study of effect of pre-treatment conditions and the benzene adsorption. J. Mol. Catal. A Chem. 201, 223–235.
Wang, Z.-Y., Zhang, L.-P., Yang, Y.-X., 2009. Structural investigation of some important Chinese diatomites. Glas. Phys. Chem. 35, 673–679.
Wang, Y., Lin, X., Wen, K., Zhu, J., He, H., 2015. Effects of organic templates on the structural properties of porous clay heterostructures: a non-micellar template model for porous structure. J. Porous. Mater. 22, 219–228.
Wu, P., Wu, H., Li, R., 2005. The microstructural study of thermal treatment montmorillonite from Heping, China. Spectrochim. Acta A 61, 3020–3025.
Yoon, Y.H., Nelson, J.H., 1984. Application of gas adsorption kinetics. I. A theoretical model for respirator cartridge service life. J. Am. Ind. Hyg. Assoc. 45, 509–516.
Yu, W., Deng, L., Yuan, P., Liu, D., Yuan, W., Liu, P., He, H., Li, Z., Chen, F., 2015a. Surface silylation of natural mesoporous/macroporous diatomite for adsorption of benzene. J. Colloid Interface Sci. 448, 545–552.
Yu, W., Yuan, P., Liu, D., Deng, L., Yuan, W., Tao, B., Cheng, H., Chen, F., 2015b. Facile preparation of hierarchically porous diatomite/MFI-type zeolite composites and their performance of benzene adsorption: the effects of NaOH etching pretreatment. J. Hazard. Mater. 285, 173–181.
Yuan, P., 2016. Thermal-treatment-induced deformations and modification of halloysite. In: Yuan, P., Thill, A., Bergaya, F. (Eds.), Nanosized Tubular Clay Minerals. Elsevier, Amsterdam, pp. 137–166 (Chapter 7).
Yuan, P., Southon, P.D., Liu, Z., Green, M.E., Hook, J.M., Antill, S.J., Kepert, C.J., 2008. Functionalization of halloysite clay nanotubes by grafting with γ-aminopropyltriethoxysilane. J. Phys. Chem. C 112, 15742–15751.
Yuan, P., Tan, D., Annabi-Bergaya, F., Yan, W., Liu, D., Liu, Z., 2013. From platy kaolinite to aluminosilicate nanoroll via one-step delamination of kaolinite: effect of the temperature of intercalation. Appl. Clay Sci. 83-84, 68–76.
Yuan, P., Tan, D., Annabi-Bergaya, F., 2015a. Properties and applications of halloysite nanotubes: recent research advances and future prospects. Appl. Clay Sci. 112, 75–93.
Yuan, W., Yuan, P., Liu, D., Yu, W., Deng, L., Chen, F., 2015b. Novel hierarchically porous nanocomposites of diatomite-based ceramic monoliths coated with silicalite-1 nanoparticles for benzene adsorption. Microporous Mesoporous Mater. 206, 184–193.
Zhang, Y., Fu, L., Yang, H., 2012a. Insights into the physicochemical aspects from natural halloysite to silica nanotubes. Colloids Surf. A Physicochem. Eng. Asp. 414, 115–119.
Zhang, W., Qu, Z., Li, X., Wang, Y., Ma, D., Wu, J., 2012b. Comparison of dynamic adsorption/desorption characteristics of toluene on different porous materials. J. Environ. Sci. (China) 24, 520–528.
Zhao, X., Ma, Q., Lu, G., 1998. VOC removal: comparison of MCM-41 with hydrophobic zeolites and activated carbon. Energy Fuel 12, 1051–1054.